ATLAS PUB Note

ATL-DAPR-PUB-2024-001

9th September 2024

Preliminary analysis of the luminosity calibration for the ATLAS 13.6 TeV data recorded in 2023

The ATLAS Collaboration

This note presents figures and tables from the preliminary analysis of the ATLAS luminosity calibration for the data recorded in pp collisions at $\sqrt{s} = 13.6$ TeV in 2023. The tables include a detailed breakdown of the systematic uncertainties. The uncertainty of the combined 2022 and 2023 datasets is also presented.

Update 9 September 2024: Added combination of 2022 and 2023 luminosity uncertainties.

1 Introduction

This note collects figures and tables from the luminosity calibration of the $\sqrt{s}$ = 13.6 TeV pp collision data sample recorded by the ATLAS detector at the LHC in 2023.

The uncertainty in the integrated luminosity for data recorded in 2023 is 2.0%, following the methodology discussed in Ref. [1], using the LUCID-2 detector [2] for the primary luminosity measurement, complemented by measurements using the inner detector and calorimeters. The uncertainty is dominated by two effects. The first is non-linear transverse correlations, known as non-factorisation, in the bunch-density distributions during the beam-separation scans, which are used to determine the absolute luminosity scale. The second dominant effect comes from transferring this calibration from the data-taking conditions during the absolute luminosity calibration to the conditions of routine physics data-taking. Various beam-, calibration method-, consistency-, reproducibility- and stability-related effects provide smaller contributions to the overall uncertainty.

Figures related to the absolute luminosity calibration based on van-der-Meer (vdM) scans are shown in Section 2, figures and a table illustrating the calibration transfer and the long-term stability monitoring for physics data-taking are given in Section 3, and tables summarising the systematic uncertainties are shown in Section 4. Section 5 shows the error breakdown on the luminosity uncertainty for combined analyses using 2022 and 2023 data.

2 Van der Meer scans

This section presents figures that illustrate the analysis of the van der Meer (vdM) scans. In all cases the LUCID Bi2HitOR algorithm is used. This algorithm counts the total number of hits in the four LUCID Bi2 tubes on each side of the ATLAS detector. All variables shown in the figures are defined in Ref. [1]. The 2023 vdM scan period consisted of two fills of the LHC. The beam was lost after the second on-axis scan in fill 8997, and a second fill 8999 was started. The first fill contains an on-axis scan (Scan I), an off-axis scan (Scan II), a 2D grid scan (Scan III) and a second on-axis scan (Scan IV). The second fill contains an on-axis scan (Scan V), an off-axis scan (Scan VI) and another on-axis scan (Scan VII).

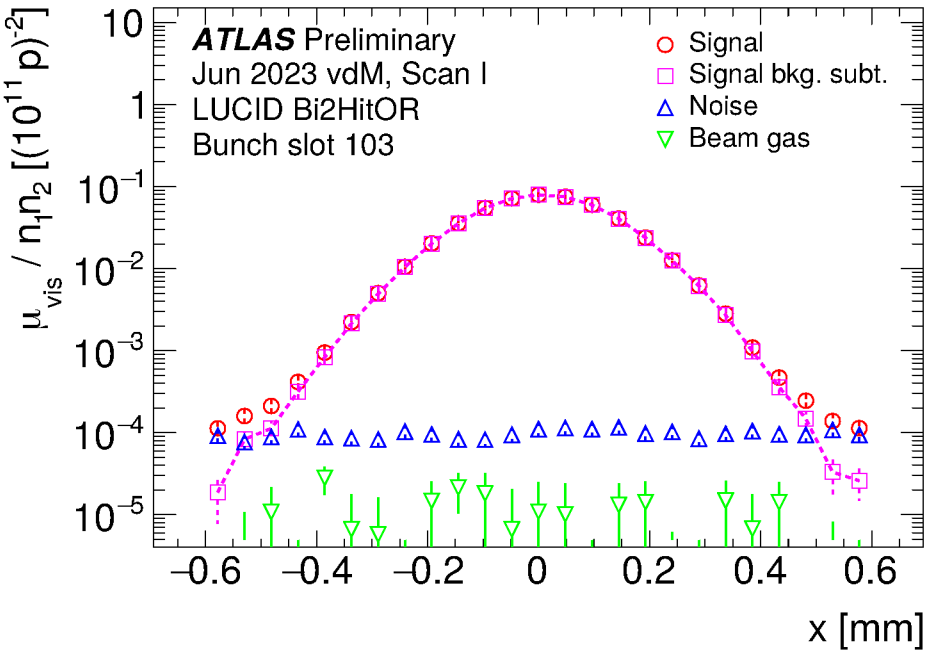

Figure 1: Visible interaction rate μ_{vis} per unit bunch population product $n_1 n_2$ vs. beam separation during a horizontal vdM scan, for bunch slot (BCID) 103 in scan I of 2023, using the LUCID Bi2HitOR algorithm. The measured rate is shown by the red circles, the background-subtracted rate by the pink squares, the estimated background from noise and afterglow by the blue upward-pointing triangles and that from beam–gas interactions by the green downward-pointing triangles. The error bars show the statistical uncertainties, which are in some cases smaller than the symbol sizes.

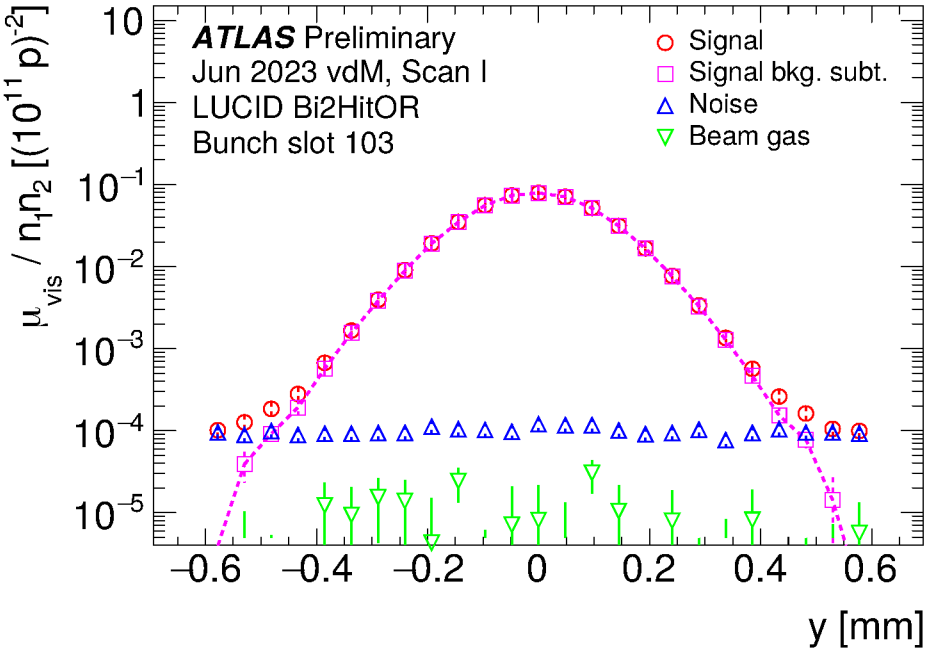

Figure 2: Visible interaction rate μ_{vis} per unit bunch population product $n_1 n_2$ vs. beam separation during a vertical vdM scan, for bunch slot (BCID) 103 in scan I of 2023, using the LUCID Bi2HitOR algorithm. The measured rate is shown by the red circles, the background-subtracted rate by the pink squares, the estimated background from noise and afterglow by the blue upward-pointing triangles and that from beam–gas interactions by the green downward-pointing triangles. The error bars show the statistical uncertainties, which are in some cases smaller than the symbol sizes.

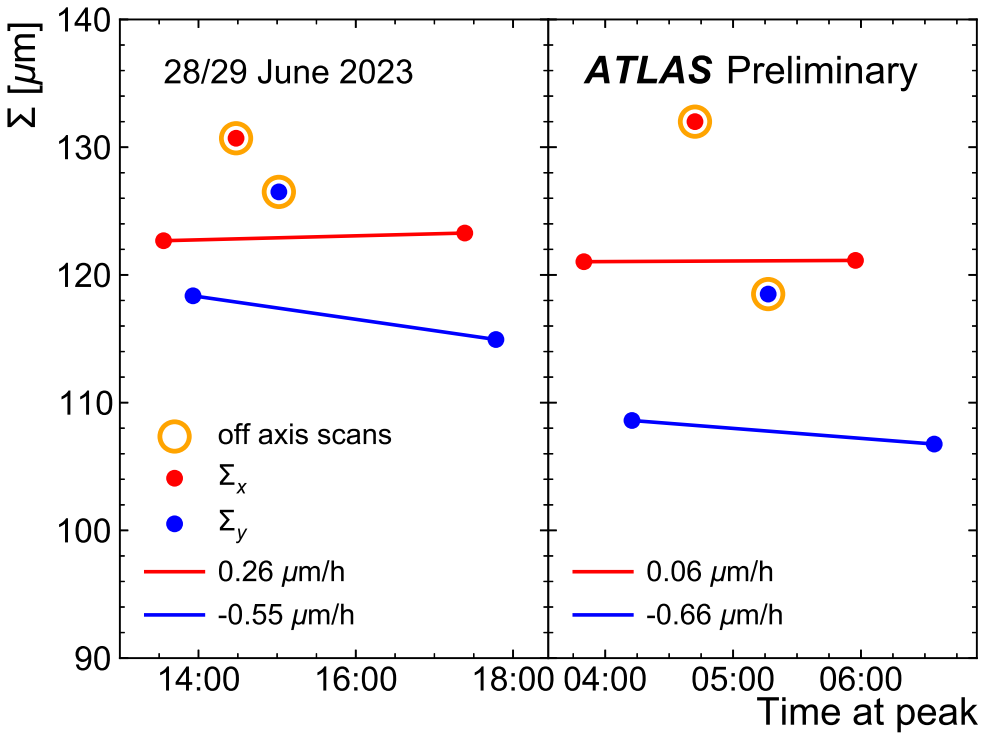

Figure 3: Time evolution of the bunch-averaged horizontal and vertical convolved beam widths (Σ) measured in two on-axis vdM-scan pairs in each of the two fills, and in two off-axis scan pairs (circled symbols) in the same fills. The points are the mean values measured over the different bunches, plotted at the time of the middle of the scan. The lines are linear fits to the on-axis data. A large deviation of the off-axis convolved width from the solid line of the same colour is indicative of a non-factorisation effect. The error bars are smaller than the symbol sizes.

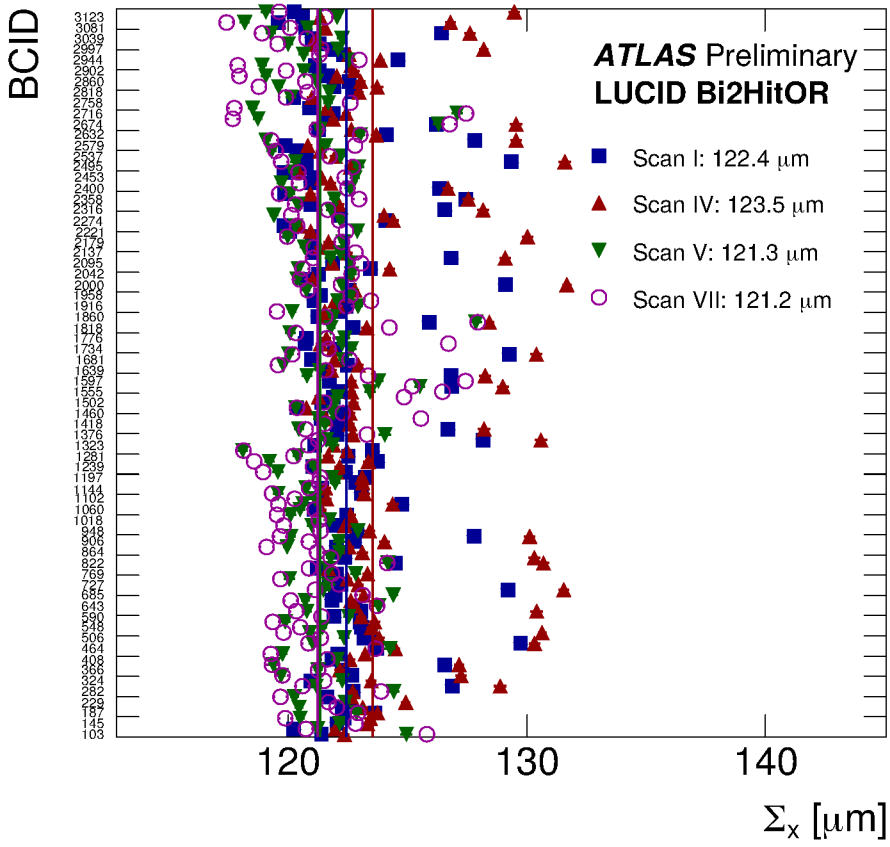

Figure 4: Bunch-by-bunch horizontal convolved beam width (Σ_x) measured in the four on-axis scan pairs. The vertical lines represent the weighted bunch-averaged value for each scan pair separately. The error bars are statistical only, and are approximately the size of the marker. The numbers given in the legend are the bunch-averaged values for each scan.

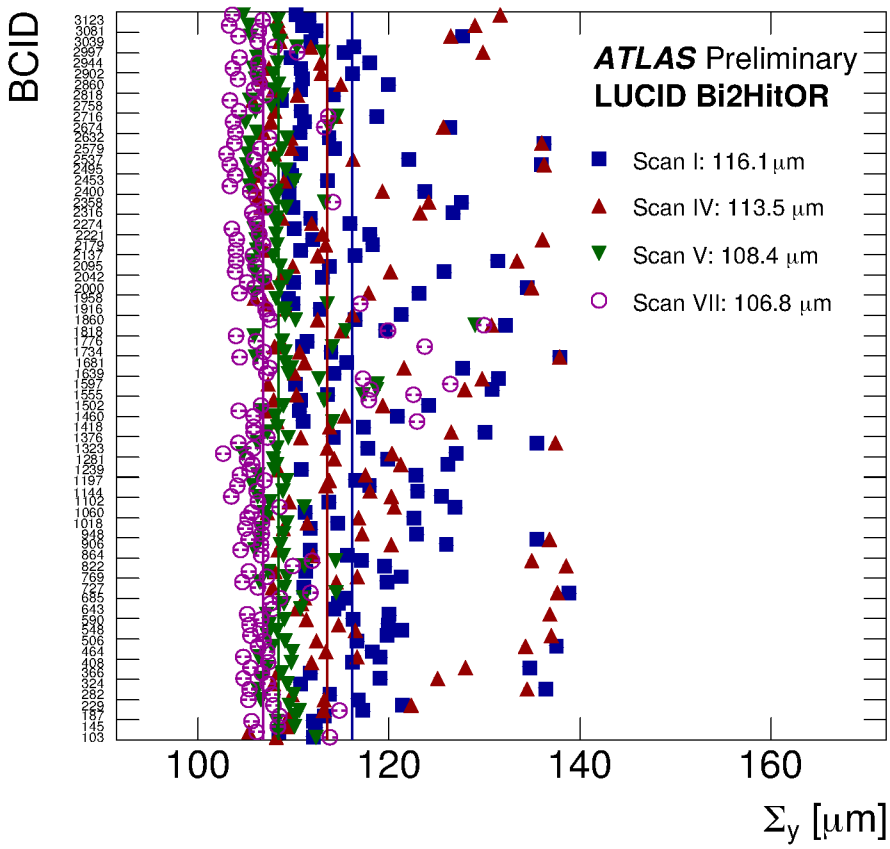

Figure 5: Bunch-by-bunch vertical convolved beam width (Σ_y) measured in the four on-axis scan pairs. The vertical lines represent the weighted bunch-averaged value for each scan pair separately. The error bars are statistical only, and are approximately the size of the marker. The numbers given in the legend are the bunch-averaged values for each scan.

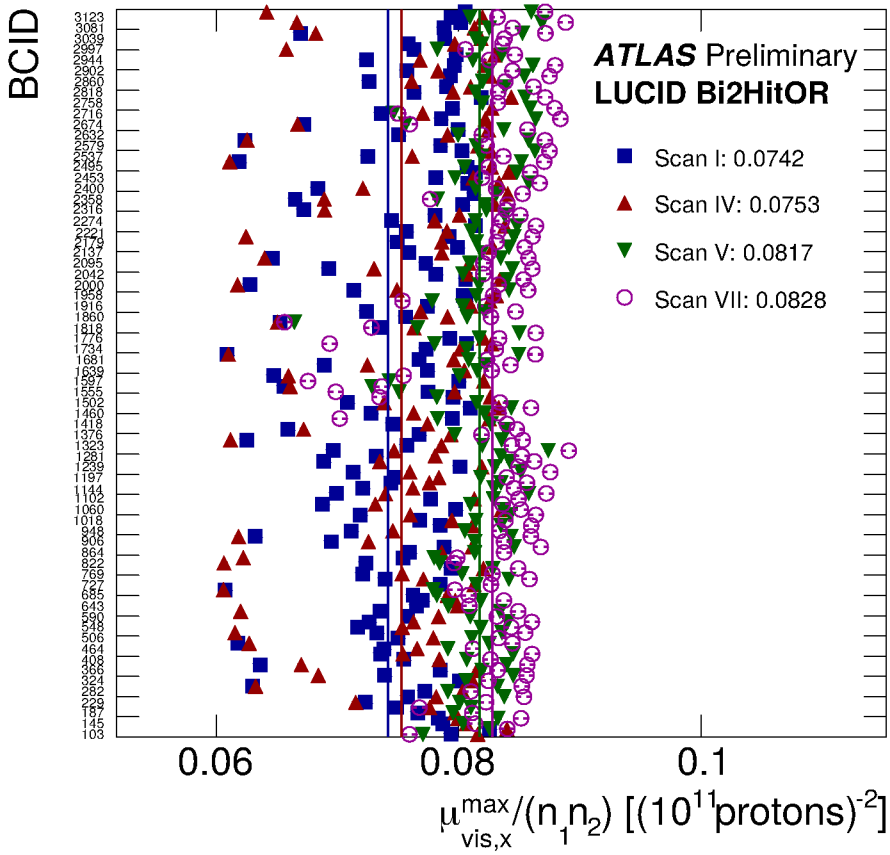

Figure 6: Bunch-by-bunch peak specific interaction rate per bunch crossing measured for the horizontal scan in the four on-axis scan pairs. The vertical lines represent the weighted bunch-averaged value for each scan pair separately. The error bars are statistical only, and are approximately the size of the marker. $\mu_{\mathrm{vis}}^{\mathrm{max}}$ denotes the maximal fitted visible interaction rate μ_{vis} over the scan. n_1, n_2 are the number of protons in the two colliding bunches in beam 1 and 2. The numbers given in the legend are the bunch-averaged values for each scan.

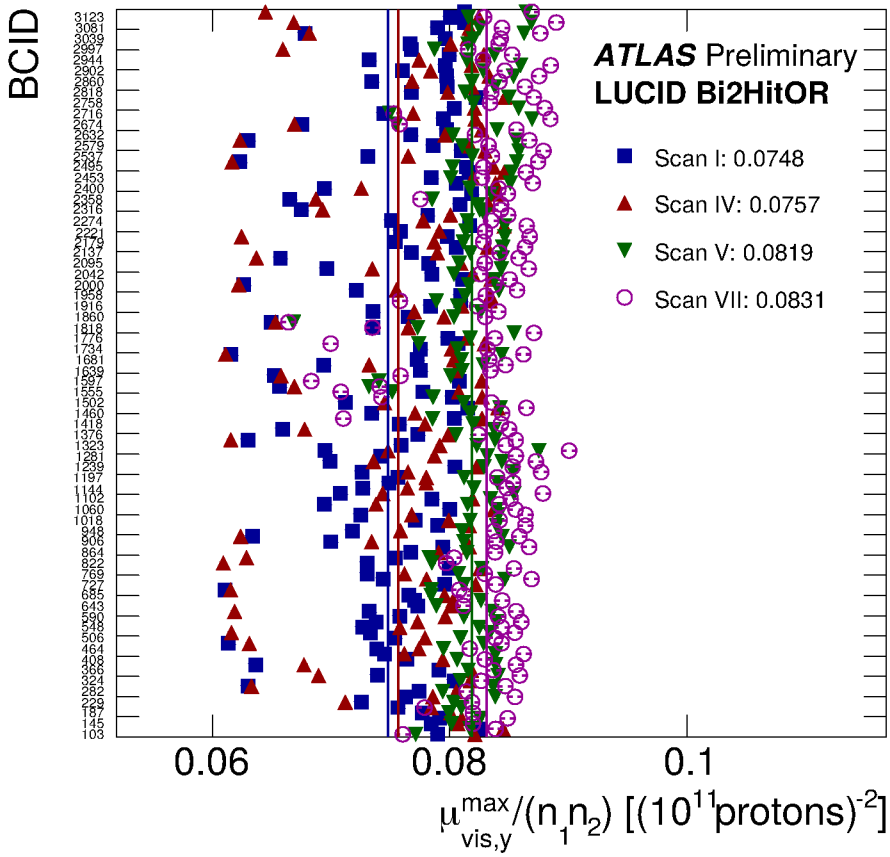

Figure 7: Bunch-by-bunch peak specific interaction rate per bunch crossing measured for the vertical scan in the four on-axis scan pairs. The vertical lines represent the weighted bunch-averaged value for each scan pair separately. The error bars are statistical only, and are approximately the size of the marker. $\mu_{\mathrm{vis}}^{\mathrm{max}}$ denotes the maximal fitted visible interaction rate μ_{vis} over the scan. n_1, n_2 are the number of protons in the two colliding bunches in beam 1 and 2. The numbers given in the legend are the bunch averaged values.

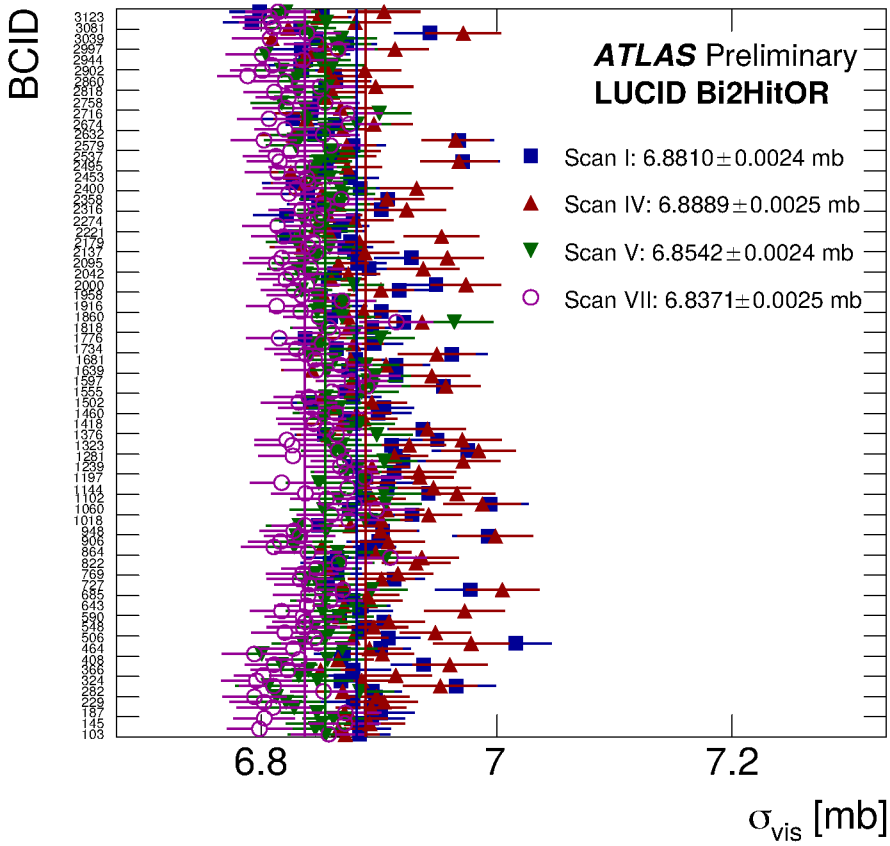

Figure 8: Fully corrected, bunch-by-bunch σ_{vis} values measured in the four on-axis scan pairs. The error bars are statistical only. The vertical lines represent the weighted bunch-averaged visible cross-section, separately for each scan pair. The numbers given in the legend are the bunch-averaged values for each scan and their statistical errors.

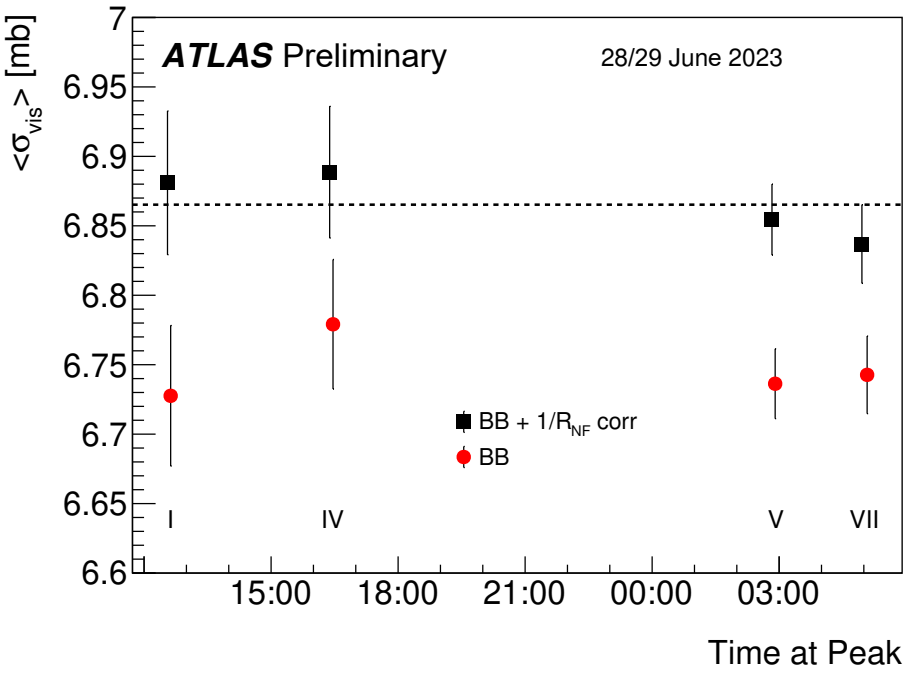

Figure 9: Visible cross-section σ_{vis} measured in the four on-axis scan pairs, as a function of time in the vdM-calibration session, after background and beam-beam (BB) correction, and either before (red circles) or after (black squares) non-factorisation (NF) correction. Scan pairs I and IV (resp. V and VII) were recorded in LHC fill 8997 (resp. 8999). The horizontal dashed line represents the non-factorisation-corrected σ_{vis} value averaged over the four scans. All σ_{vis} values shown refer to the average over all 136 bunches, whereas the non-factorisation correction is obtained only from the 12 bunches for which luminous-region data are available. The error bars show the RMS spread across the 136 bunches. The horizontal axis shows the time half-way between that of the peaks of the horizontal and the vertical scan. The Roman numerals in the figure refer to the number of the on-axis scan pairs.

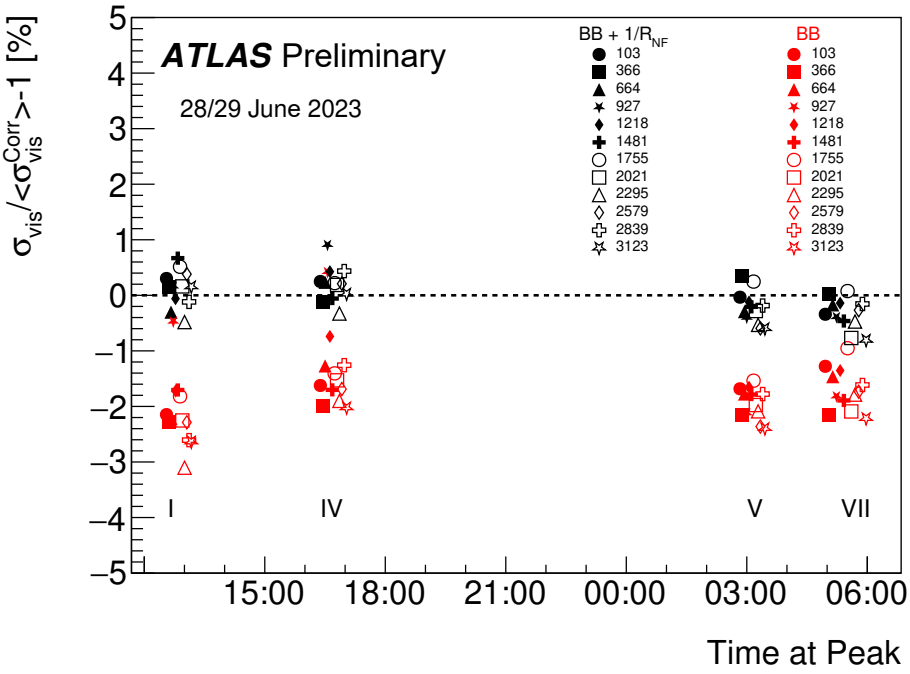

Figure 10: Fractional deviation of the bunch-by-bunch visible cross-section σ_{vis} measured in the four on-axis scan pairs relative to the fully corrected value averaged over all scans and all 136 colliding bunches, as a function of time in the vdM-calibration session, after background and beam-beam (BB) correction, and either before (red symbols) or after (black symbols) non-factorisation (NF) correction. Scan pairs I and IV (resp. V and VII) were recorded in LHC fill 8997 (resp. 8999). Each of the twelve shapes (open or filled squares, circles, triangles, etc) is associated with a specific colliding-bunch pair for which luminous-region data are available; the corresponding bunch-crossing identifier (BCID) is indicated next to the symbol. On the horizontal axis, each cluster of symbols is centred on the time half-way between the peaks of the horizontal and vertical scans. The Roman numerals in the figure refer to the number of the on-axis scan pairs.

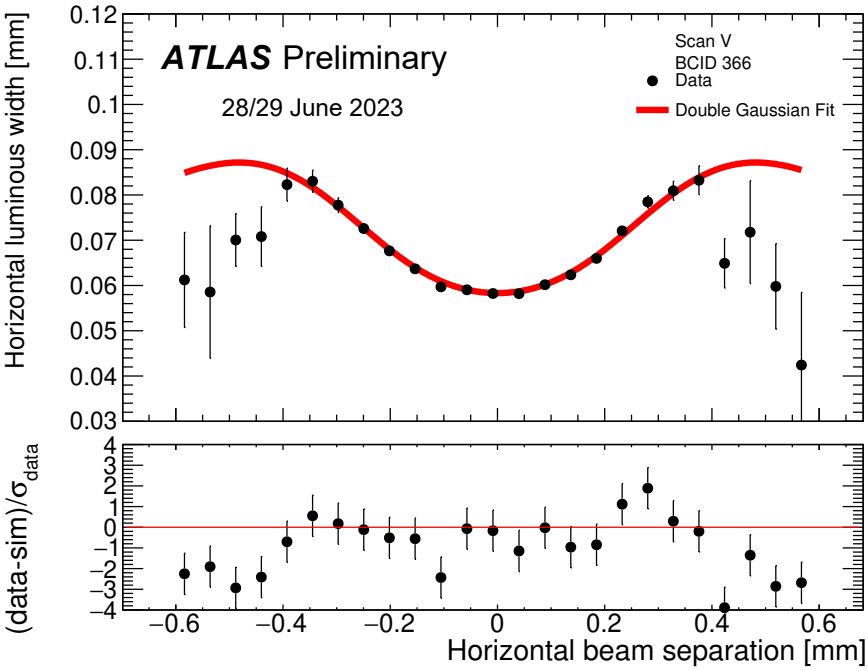

Figure 11: Beam-separation dependence of the horizontal RMS luminous width for BCID 366 during the horizontal vdM scan V. The red line is the result of the combined-offset Luminous-Region-Evolution (LRE) fit using a non-factorisable, three-dimensional double-Gaussian model for each bunch. The LRE fit models the two beams individually using the vdM scan data as well as the beamspot position and width.

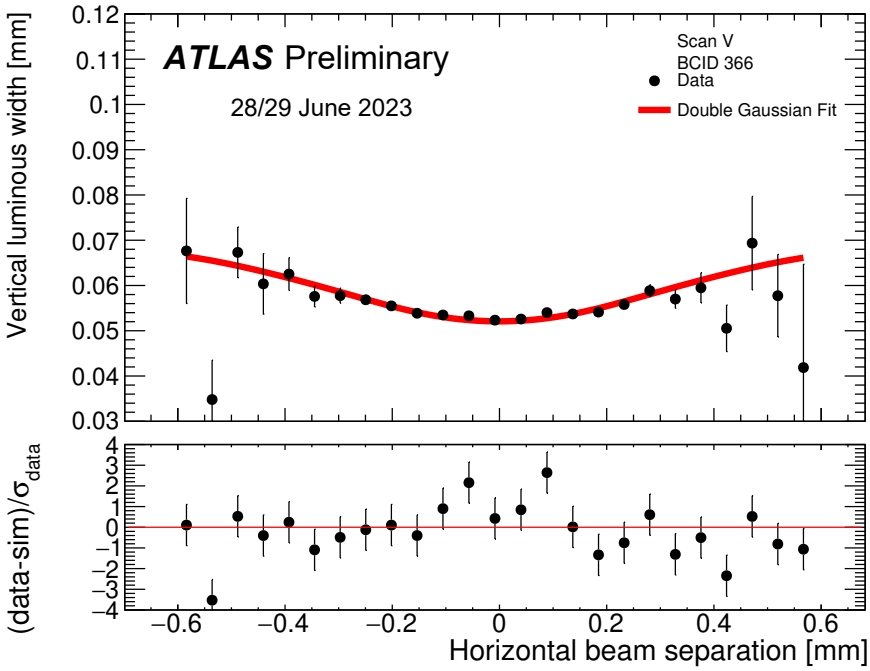

Figure 12: Beam-separation dependence of the vertical RMS luminous width for BCID 366 during horizontal vdM scan V. The red line is the result of the combined-offset LRE fit using a non-factorisable, three-dimensional double-Gaussian model for each bunch. The LRE fit models the two beams individually using the vdM scan data as well as the beamspot position and width.

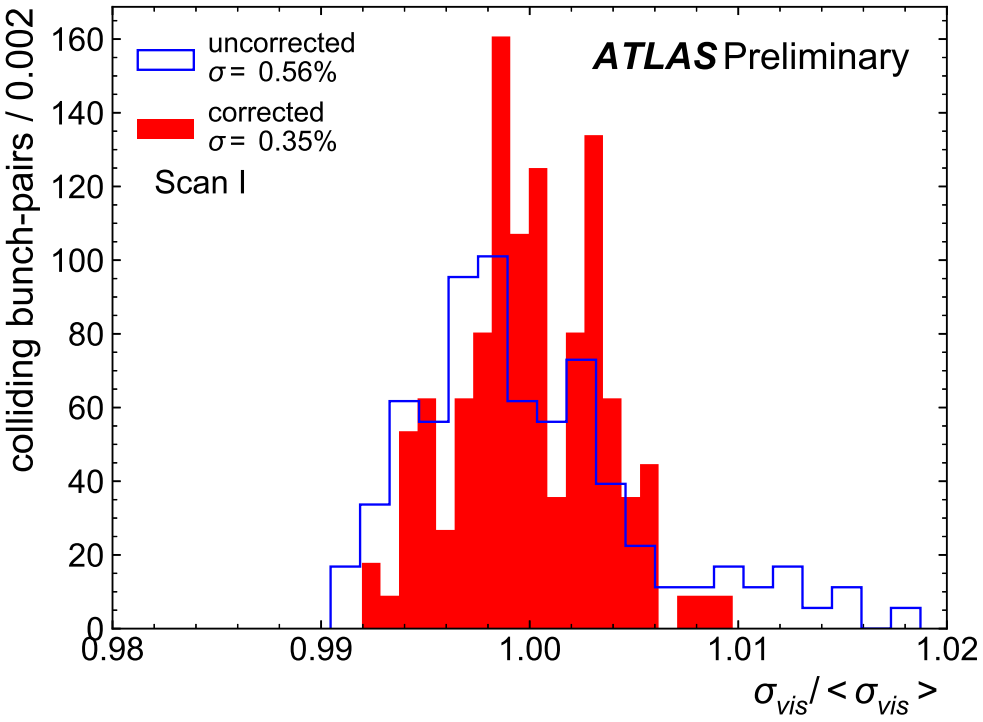

Figure 13: Normalised σ_{vis} values for the 136 colliding bunches in scan I. The open blue histogram shows the values after all corrections apart from non-factorisation. The filled red histogram shows the same values after they have been corrected bunch-by-bunch using the x-y grid scan (scan III), under the assumption that the non-factorisation bias does not vary significantly between scans I and III. The bunch-to-bunch spread is observed to significantly narrow as a result of the bunch-by-bunch non-factorisation correction.

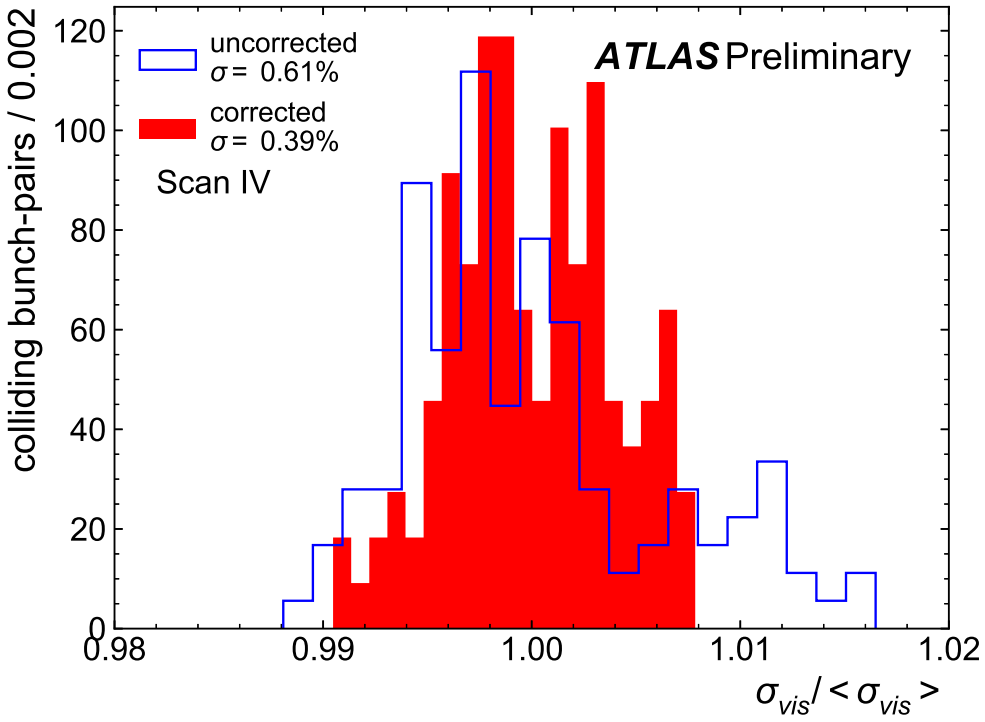

Figure 14: Normalised σ_{vis} values for the 136 colliding bunches in scan IV. The open blue histogram shows the values after all corrections apart from non-factorisation. The filled red histogram shows the same values after they have been corrected bunch-by-bunch using the x-y grid scan (scan III), under the assumption that the non-factorisation bias does not vary significantly between scans III and IV. The bunch-to-bunch spread is observed to significantly narrow as a result of the bunch-by-bunch non-factorisation correction.

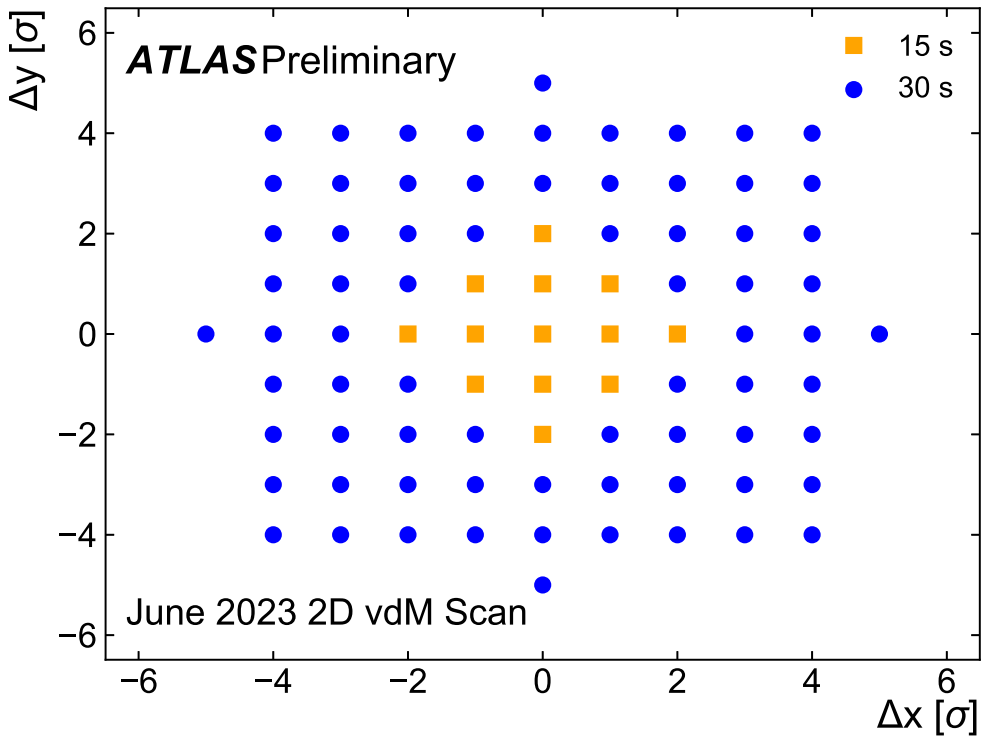

Figure 15: Scanning grid for the generalised, two-dimensional vdM scan performed during the 2023 vdM session. The axes indicate the horizontal (Δx) and vertical (Δy) nominal separation between the beams, in units of the nominal single-beam width σ. Luminosity data were recorded for 15 s or 30 s per scan step at small (orange squares) or large (blue circles) beam separation respectively, to improve the statistical precision in the tails of the scan.

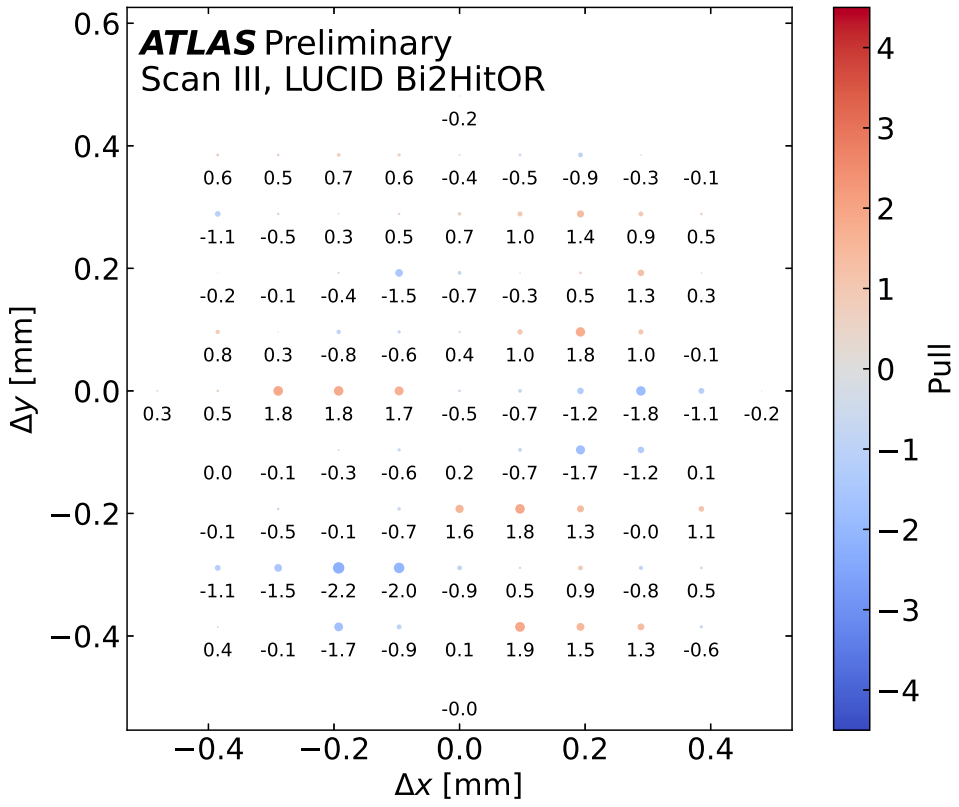

Figure 16: Pulls of a two-dimensional GP6 fit averaged over the bunches of the grid scan. The GP6 function is defined as $\mathrm{gp6}(x,y) = \mu \exp(-(x_n^2 + y_n^2 + \kappa x_n y_n)/2)((1. + c_{2x}x_n^2 + c_{4x}x_n^4 + c_{6x}x_n^6)(1. + c_{2y}y_n^2 + c_{4y}y_n^4 + c_{6y}y_n^6) + c_{2x2y}x_n^2y_n^2 + c_{4x2y}x_n^4y_n^2 + c_{2x4y}x_n^2y_n^4)$ with $x_n = \frac{x-x_m}{\sigma_x}$, $y_n = \frac{y-y_m}{\sigma_y}$. The fit parameters are the peak value μ, the Gaussian widths σ_x, σ_y, the coupling term in the Gaussian function κ, the polynomial coefficients c_i and the mean values of the Gaussian function, x_m, y_m. The fit is performed on a bunch-by-bunch basis and the shown pulls are the bunch-averaged values.

3 Calibration-transfer and long-term stability studies

The calibration transfer from the vdM regime to data-taking conditions of physics running, as well as its uncertainty for this preliminary calibration, are shown in Figure 17 and Table 1, respectively. The long-term stability in 2023 data-taking is displayed in Figures 18–21.

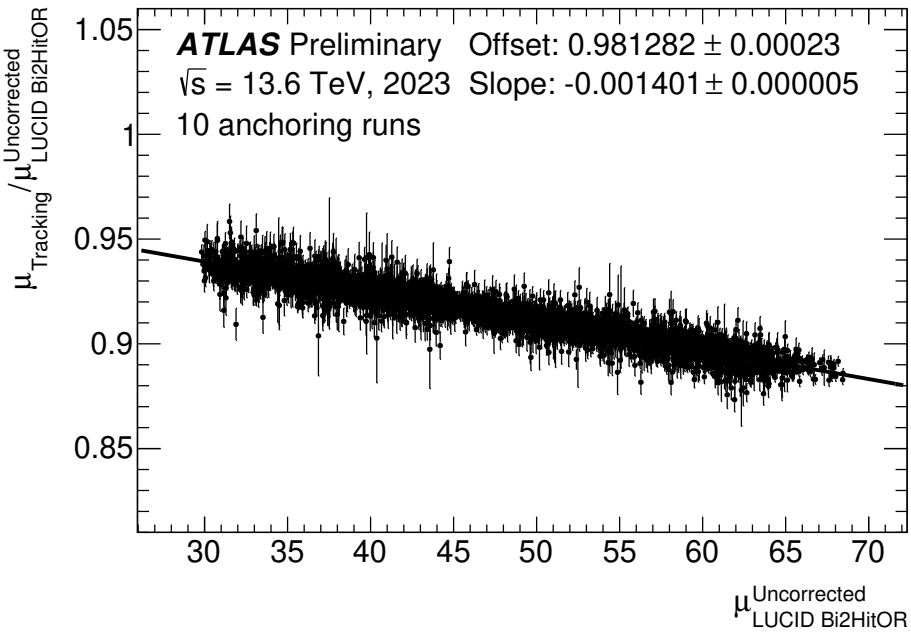

Figure 17: Ratio of the bunch-averaged pile-up parameter μ_{Tracking}, reported by the track-counting luminosity algorithm (denoted as Selection A in Ref. [1]), to $\mu_{\text{LUCID Bi2HitOR}}$, obtained using the LUCID Bi2HitOR algorithm before any pile-up correction, as a function of the bunch-averaged pile-up parameter $\mu_{\text{LUCID Bi2HitOR}}$. Data from ten physics fills surrounding the vdM fill are included. The μ-dependence of the LUCID response is parameterised by a straight-line fit (solid black line), which is used to correct the LUCID luminosity on a minute-by-minute basis during 2023 data-taking. This correction amounts to approximately -0.14% per unit of μ.

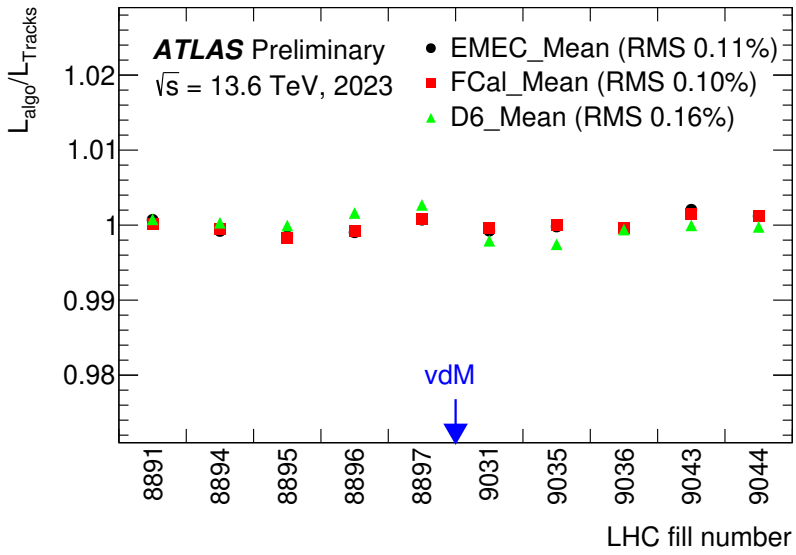

Figure 18: Ratios of the per-fill integrated luminosity measured by the electromagnetic endcap calorimeter (EMEC_Mean), by the electromagnetic forward calorimeter (FCal_Mean) and by the D6-cells of the TILE calorimeter (D6_Mean), to that measured by track-counting (denoted as Selection A in Ref. [1]) in ten physics fills surrounding the vdM fill, as function of the LHC fill number. The EMEC, the FCal and the TILE D6-cells measurements are averages of the respective A-side and C-side algorithms. The vdM fill is indicated by the blue arrow. The ratios are normalised such that the average over all ten fills is unity. The legends show the RMS difference between the calorimeter and track-counting measurements in each case. The largest RMS across the calorimeter subsystems sets the calibration-anchoring uncertainty (0.16%).

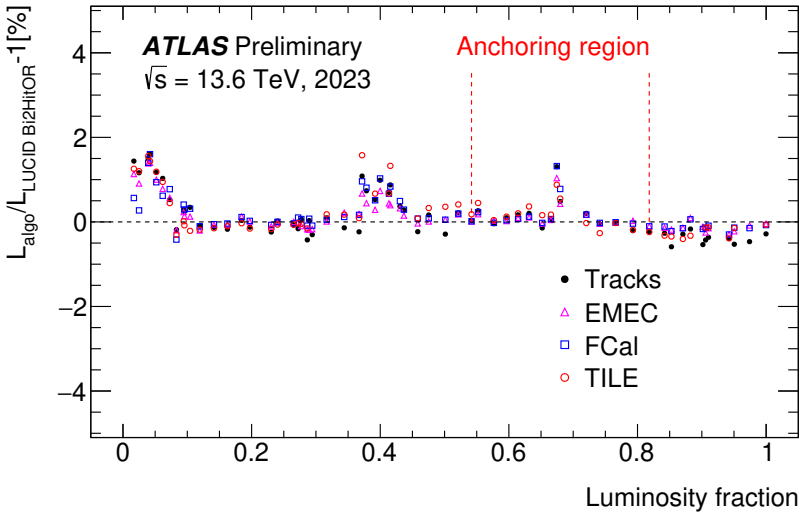

Figure 19: Fractional differences in fill-integrated luminosity between the LUCID Bi2HitOR luminosity measurements and the EMEC, the FCal, the TILE and the track-counting luminosity algorithm (denoted as Selection A in Ref. [1]), as a function of the fractional cumulative integrated luminosity in 2023. The EMEC, the FCal and the TILE D6-cells measurements are averages of the respective A-side and C-side algorithms. The anchoring region marks the range of ten fills around the vdM fill used to normalise the calorimeter measurements to track-counting and to evaluate the μ-correction parameters used for the calibration of LUCID to track-counting during physics data-taking. The selection of fills is restricted to those passing standard data-quality requirements.

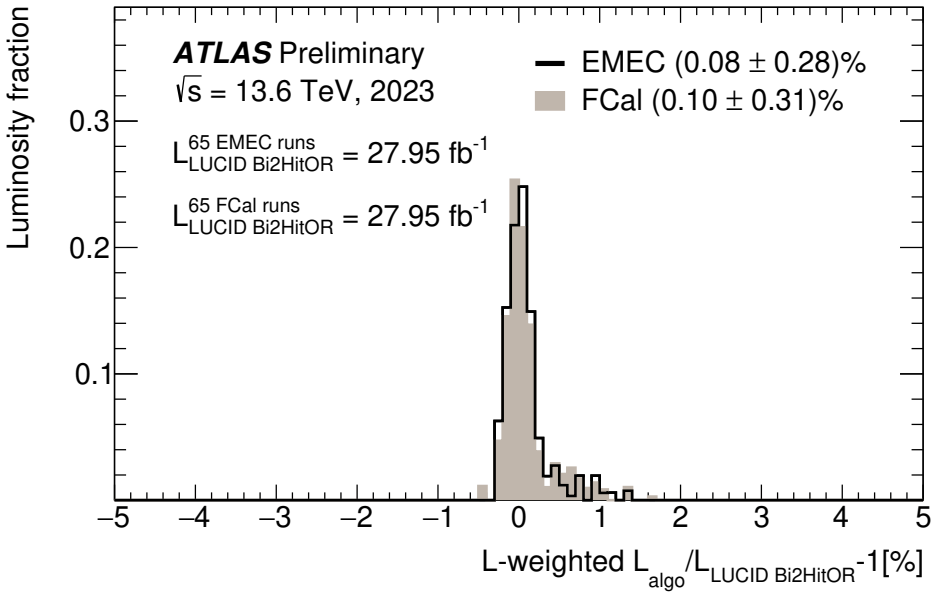

Figure 20: Distributions of relative differences in fill-integrated luminosity between the EMEC and FCAL luminosity measurements (A-side and C-side averages) and the baseline LUCID Bi2HitOR luminosity measurement, weighted by the integrated luminosity in each fill, for 2023. The selection of fills is restricted to those passing standard data-quality requirements; the quoted integrated luminosity is the one delivered by the LHC, not corrected for ATLAS detector and trigger readiness. The mean and RMS values for each algorithm are indicated in the legend. The largest mean deviation across the calorimeter subsystems and track counting (Figures 20–21) sets the long-term stability uncertainty.

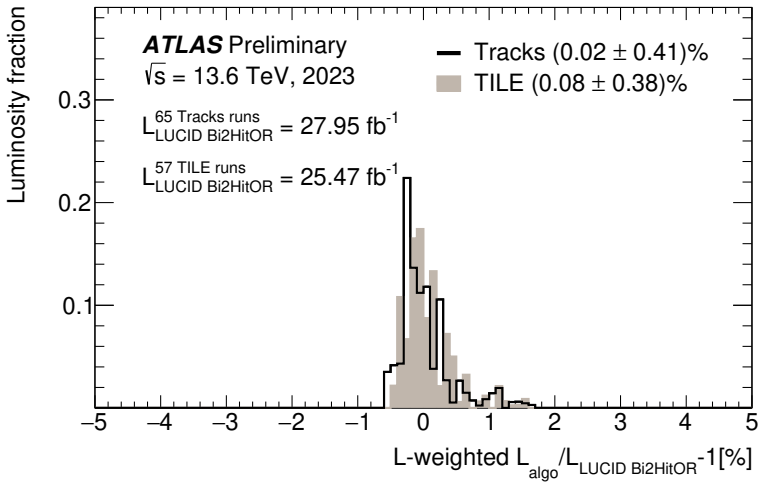

Figure 21: Distributions of relative differences in fill-integrated luminosity between the FCal (A-side and C-side average) and track counting luminosity measurements and the baseline LUCID Bi2HitOR luminosity measurement, weighted by the integrated luminosity in each fill, for 2023. The selection of fills is restricted to those passing standard data-quality requirements; the quoted integrated luminosity is the one delivered by the LHC, not corrected for ATLAS detector and trigger readiness. The mean and RMS values for each algorithm are indicated in the legend. The largest mean deviation across the calorimeter subsystems and track counting (Figures 20 and 21) sets the long-term stability uncertainty.

3.1 Uncertainty on the calibration transfer

The uncertainty for the calibration transfer is shown in Table 1 and Figures 22 - 24.

Extrapolation of luminosity calibration	**Used cell families**	**Range of shifts across used cell families**
1-step extrapolation		
($\mu \approx 0.5$, 140b, isolated) $\rightarrow$ ($\mu \approx 40$, 898b, trains)	E3, E4, A13, A14	[0.5, 1.1]‰
Alternative: 2-step extrapolation		
($\mu \approx 0.5$, 140b, isolated) $\rightarrow$ ($\mu \approx 60$, 140b, isolated)	E3, E4, A13, A14	[-0.7, -0.3]‰
($\mu \approx 60$, 140b, isolated) $\rightarrow$ ($\mu \approx 40$, 898b, trains) (*)	E3, E4, A13, A14	[0.7, 1.3]‰
Combined 2-step extrapolation		[0.0, 1.0]‰
Upper limit on total extrapolation impact		**< 1.1‰**

Table 1: Range of shifts in the ratios of the Tile-calorimeter luminosity and the track-counting luminosity (denoted as Selection A in Ref. [1]) in LHC fills 9007 and 9019, with increasing bunch-averaged pile-up parameter (μ), and moving from isolated bunches to bunch trains. These ranges of shifts probe the linearity of the track-counting algorithm, which is used in Figure 17 to extrapolate the absolute LUCID calibration from the vdM regime (low-μ, low number of bunches, isolated bunches) to the data-taking conditions of physics running (high-μ, large number of bunches, bunch trains). The fills are selected and compared such that either both running conditions are modified (1-step extrapolation), or only one at a time (2-step extrapolation). The comparison of track-counting is done to different Tile cell families, corresponding to different regions in the ATLAS Tile calorimeter. The Tile cell families used to obtain the range of shifts are indicated for each extrapolation step. The Tile data has been corrected for residual ambient activation, except for one extrapolation step indicated with (*), where at high μ-values the bias from the activation is considered small. The rounded maximum shifts are used as an upper limit on the impact of the extrapolation on the luminosity calibration. The upper limit on the total impact of the extrapolation from the vdM to the regime of physics data-taking is symmetrised and considered as calibration transfer uncertainty.

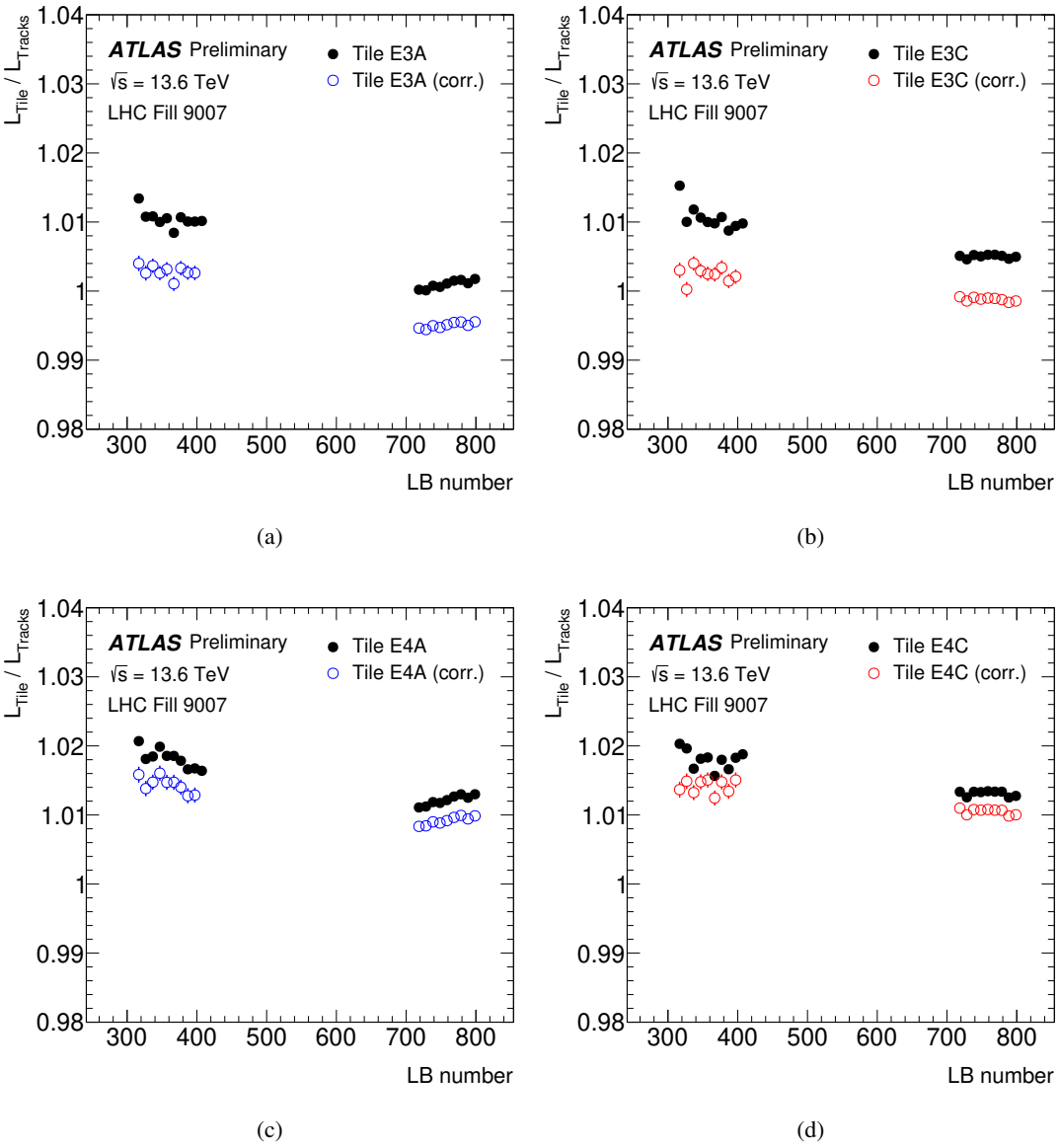

Figure 22: Ratios of Tile E-cell luminosity measurements to those from track-counting for the E3 cell families on the (a) A-side and (b) C-side and the E4 cell families on the (c) A-side and (d) C-side, as a function of luminosity block number, in two periods of steady-state running at low and high pileup in LHC fill 9007 with 140 isolated bunches. The ratios are shown for Tile data corrected for residual ambient activation (blue or red open circles) and Tile data without any activation correction (black filled circles). The ratios have been averaged over ten consecutive luminosity blocks. The shift in the activation-corrected ratio between the two groups of luminosity blocks corresponds to the first part of the 2-step extrapolation in Table 1.

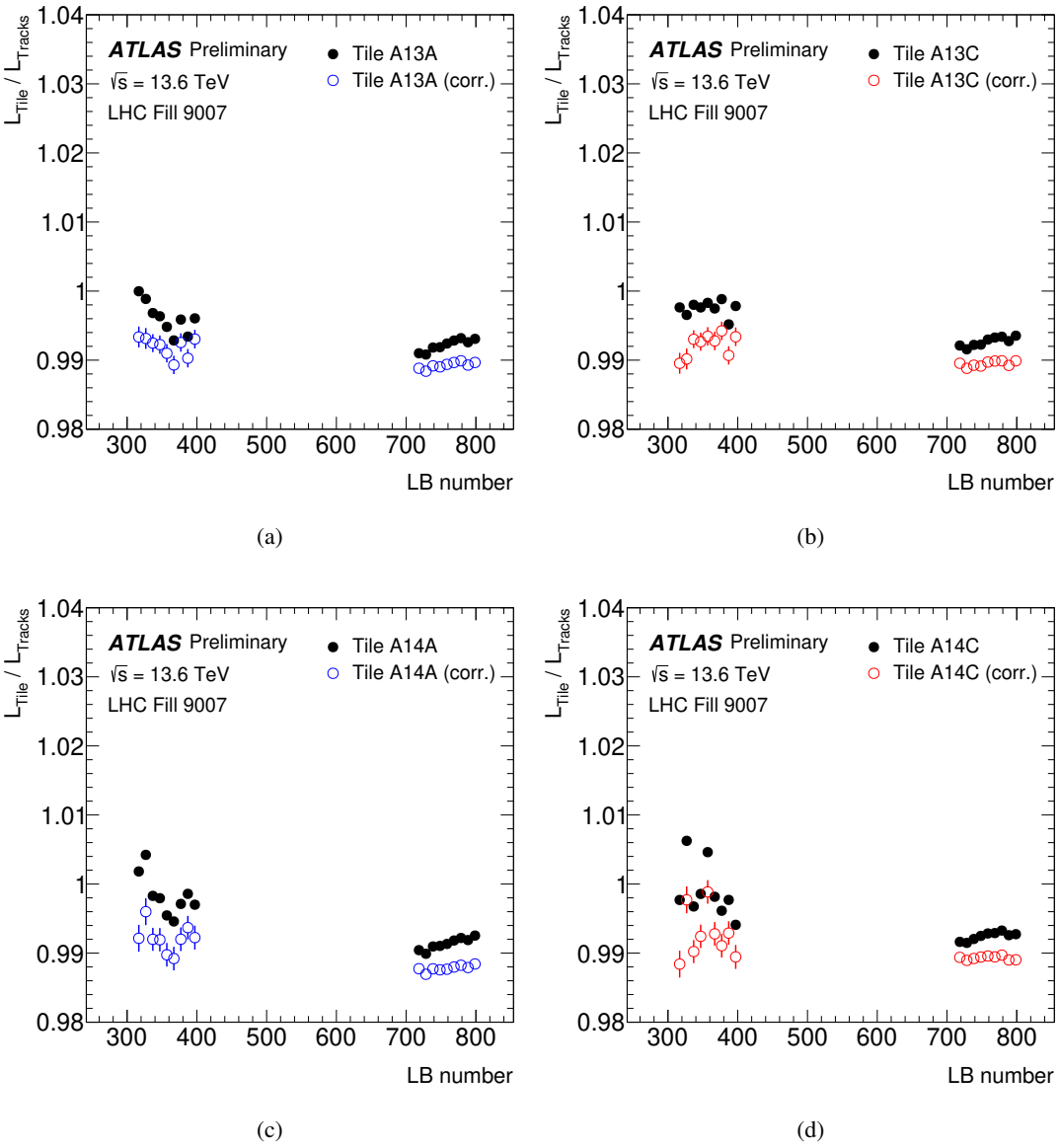

Figure 23: Ratios of Tile A-cell luminosity measurements to those from track-counting for the A13 cell families on the (a) A-side and (b) C-side and the A14 cell families on the (c) A-side and (d) C-side, as a function of luminosity block number, in two periods of steady-state running at low and high pileup in LHC fill 9007 with 140 isolated bunches. The ratios are shown for Tile data corrected for residual ambient activation (blue or red open circles) and Tile data without any activation correction (black filled circles). The ratios have been averaged over ten consecutive luminosity blocks. The shift in the activation-corrected ratio between the two groups of luminosity blocks corresponds to the first part of the 2-step extrapolation in Table 1.

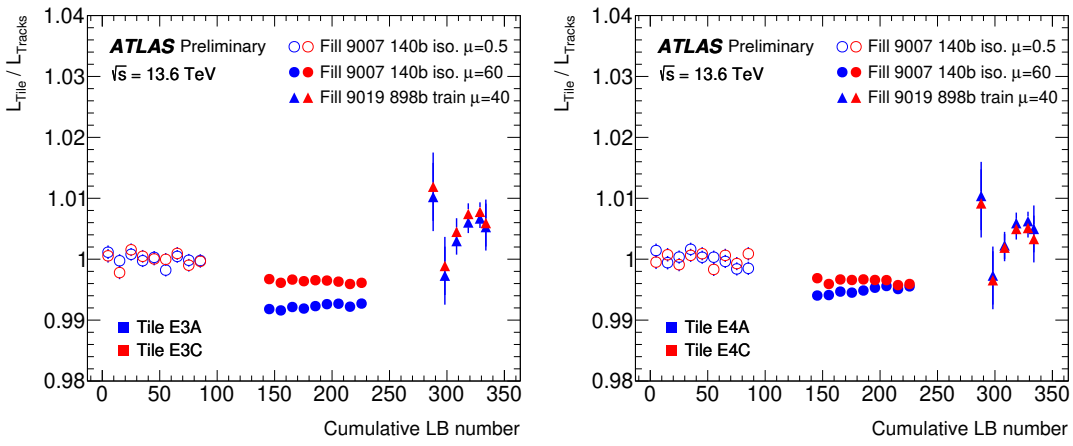

(a)

(b)

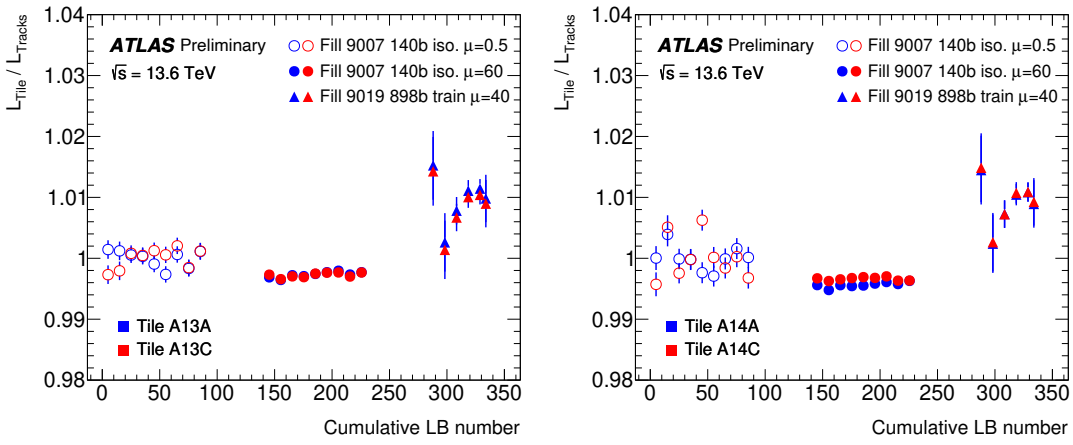

(c)

(d)

Figure 24: Ratios of luminosity measured by the Tile (a) E3 cells, (b) E4 cells, (c) A13 cells and (d) A14 cells to that measured by track counting in two periods of steady-state running at low and high pileup in LHC fill 9007 with 140 isolated bunches and in LHC fill 9019 with 898 bunches in trains. The Tile data has been corrected for residual ambient activation in both fills. Within each plot, the ratios are shown as a function of luminosity block number, with gaps between fills to give a continuous sequence over related fills. Periods with no ratio measurements within fills are not shown, and are omitted in the luminosity block numbering. The ratios have been renormalised separately for each cell family in each sequence so that the integrated ratios in the low-luminosity period of the fill 9007 are unity. The numbers of colliding bunch pairs in ATLAS and the typical μ values are indicated for each fill, and the various fill periods are plotted with different marker styles. The shift in the ratio from the period in fill 9007 with $\mu = 0.5$ to fill 9019 corresponds to the 1-step extrapolation in Table 1.

4 Systematic uncertainties

The systematic uncertainty on the integrated luminosity for the data sample from 2023 as well as a breakdown of the uncertainties are given in Table 2. The absolute integrated luminosity and uncertainty numbers are quoted in Table 3, using datasets based on data-quality requirements for four different trigger configurations. The relative uncertainty is independent of the specific data-quality selection and rounded to 2.0%.

Source	Relative Uncertainty	Total
vdM statistical uncertainty	< 0.01	
Scan-to-scan reproducibility	0.35%	
Bunch-to-bunch σ_{vis} consistency	0.36%	
Fit model	0.15%	
Background subtraction	0.30%	
Reference specific luminosity	0.44%	
Orbit drift correction	0.34%	
μ dependence	0.30%	
Beam-beam effects	0.32%	
Beam position jitter	< 0.01%	
Emittance variations	0.06%	
Factorised vdM analysis subtotal		0.93%
Non-factorisation	1.39%	
Length scale calibration (stat)	0.02%	
Absolute inner detector length scale	0.12%	
Magnetic non-linearity	0.28%	
Scan subtotal		1.70%
DCCT calibration	0.20%	
Bunch charge product	< 0.01%	
Ghost and satellite charges	0.04%	
vdM total		1.71%
Calibration transfer	1.1%	
Calibration anchoring	0.16%	
Long-term stability	0.1%	
Luminosity total		2.04%

Table 2: Systematic uncertainties associated with the preliminary luminosity calibration of the 2023 pp data sample at $\sqrt{s} = 13.6$ TeV. The fractional systematic uncertainty is broken down into four main contributions: absolute vdM calibration (detailed per uncertainty source, and subtotal), the calibration transfer from the vdM to the physics regime, calibration anchoring of the calorimeters for physics runs, and long-term stability of the luminometer response.

Trigger sets for data-quality requirements	Integrated Luminosity [fb^{-1}]
Jet triggers	25.59 ± 0.51
e/γ or non-isolated tau at L1	27.06 ± 0.54
Other triggers	27.58 ± 0.55
Jet triggers with non-standard thresholds	26.12 ± 0.52

Table 3: Integrated luminosity and systematic uncertainty, associated with the preliminary luminosity calibration of the 2023 pp data sample at $\sqrt{s}$ = 13.6 TeV for four datasets. These datasets are defined according to data quality requirements for four different trigger configurations.

5 Combination of 2022 and 2023 luminosity uncertainties

Table 4 shows the combination of the luminosity uncertainties from 2022 [3] and 2023. The correlation model follows as closely as possible the one used in run 2 [1] and is explained in the caption. The uncertainty of the 2022/2023 luminosity should be quoted as $\frac{\Delta\mathcal{L}}{\mathcal{L}} = 2.0\%$. For the central value of the luminosity the sum of the two individual years should be used.

Data sample	2022	2023	Comb.
Integrated luminosity [fb^{-1}]	31.40	27.58	58.98
Total uncertainty [fb^{-1}]	0.69	0.56	1.16
Uncertainty contributions [%]:			
Statistical uncertainty	0.01	0.01	0.01
Fit model*	0.24	0.15	0.20
Background subtraction*	0.06	0.30	0.17
FBCT bunch-by-bunch fractions*	0.01	0.01	0.01
Ghost-charge and satellite bunches†	0.17	0.04	0.11
DCCT calibration*	0.20	0.20	0.20
Orbit-drift correction	0.06	0.34	0.16
μ-dependence	0.00	0.30	0.14
Beam position jitter	0.00	0.01	0.01
Non-factorisation effects*	1.07	1.39	1.22
Beam–beam effects*	0.35	0.32	0.34
Emittance damping correction*	0.21	0.06	0.14
Length scale calibration	0.03	0.02	0.02
Inner detector length scale*	0.12	0.12	0.12
Magnetic non-linearity*	0.32	0.28	0.30
Bunch-by-bunch σ_{vis} consistency	0.50	0.36	0.31
Scan-to-scan reproducibility	0.27	0.35	0.22
Reference specific luminosity*	0.43	0.44	0.43
Subtotal vdM calibration	1.44	1.71	1.49
Calibration transfer†	1.50	1.10	1.23
Calibration anchoring	0.53	0.16	0.29
Long-term stability	0.41	0.10	0.22
Total uncertainty [%]	2.19	2.04	1.97

Table 4: Combination of the preliminary luminosity from 2022 [3] and 2023. The entries marked with * are assumed to be fully correlated, the entries marked with † are partially correlated and the others are uncorrelated. "Ghost-charge and satellite bunches" are partially correlated because ghost charge and satellite charge are correlated separately. For "Calibration transfer" a component of 1.0% due to the missing Tile calorimeter laser correction in 2022 is not correlated with 2023.

References

[1] ATLAS Collaboration,
Luminosity determination in pp collisions at $\sqrt{s} = 13$ TeV using the ATLAS detector at the LHC,
Eur. Phys. J. C **83** (2023) 982, arXiv: 2212.09379 [hep-ex] (cit. on pp. 2, 19, 20, 22, 28).

[2] G. Avoni et al., *The new LUCID-2 detector for luminosity measurement and monitoring in ATLAS*,
JINST **13** (2018) P07017 (cit. on p. 2).

[3] ATLAS Collaboration,
Preliminary analysis of the luminosity calibration of the ATLAS 13.6 TeV data recorded in 2022,
ATL-DAPR-PUB-2023-001, 2023, URL: https://cds.cern.ch/record/2853525 (cit. on p. 28).